Large-Scale Synthesis of Freestanding Layer-Structured PbI$_2$ and MAPbI$_3$ Nanosheets for High-Performance Photodetection

Changyong Lan, Ruoting Dong, Ziyao Zhou, Lei Shu, Dapan Li, SenPo Yip, and Johnny C. Ho*

Recently, due to the possibility of thinning down to the atomic thickness to achieve exotic properties, layered materials have attracted extensive research attention. In particular, PbI$_2$, a kind of layered material, and its perovskite derivatives, CH$_3$NH$_3$PbI$_3$ (i.e., MAPbI$_3$), have demonstrated impressive photoresponsivities for efficient photodetection. Herein, the synthesis of large-scale, high-density, and freestanding PbI$_2$ nanosheets is demonstrated by manipulating the microenvironment during physical vapor deposition. In contrast to conventional two-dimensional (2D) growth along the substrate surface, the essence here is the effective nucleation of microplanes with different angles relative to the in-plane direction of underlying rough-surfaced substrates. When configured into photodetectors, the fabricated device exhibits a photoresponsivity of 410 mA W^{-1}, a detectivity of 3.1×10^{11} Jones, and a fast response with the rise and decay time constants of 86 and 150 ms, respectively, under a wavelength of 405 nm. These PbI$_2$ nanosheets can also be completely converted into MAPbI$_3$ materials via chemical vapor deposition with an improved photoresponsivity up to 40 A W^{-1}. All these performance parameters are comparable to those of state-of-the-art layered-material-based photodetectors, revealing the technological potency of these freestanding nanosheets for next-generation high-performance optoelectronics.

Due to the possibility of thinning down to atomically thick two-dimensional (2D) materials, the layered-structure materials with in-plane covalent bonding and weak interlayer interactions (van der Waals) have attracted extensive amounts of research attentions.[1–5] A well-known example is graphene, the monolayer form of graphite, which exhibits numerous unique physical and chemical properties, including superior carrier mobility, high thermal conductivity, linear band structure, a large surface-to-volume ratio, etc.[6–8] However, as graphene is a semimetal with a zero bandgap, its practical utilization is highly constrained.[9–11] This way, other layered-structure semiconductor nanomaterials with strong quantum confinement effects and sizable bandgaps, such as transition metal dichalcogenides (TMDs),[12] black phosphorus,[13] and 2D trichalcogenide compounds (e.g., Bi$_2$Se$_3$ and Bi$_2$Te$_3$),[14] are widely explored and found to have great potential for various technological applications.[4,5,11,15–17] In particular, monolayer-MoS$_2$-based phototransistors have been successfully demonstrated with the extraordinarily high photoresponsivity of 880 A W^{-1} at a wavelength of 561 nm along with the negligibly low dark current for high-performance photodetection.[18]

Among many layered-structure material families, layered lead-halide perovskites have many intriguing optoelectronic properties as compared to their 3D bulk counterparts, since their 2D quantum wells are uncovered and the electronic coupling among layers may be altered.[19–23] In this regard, PbI$_2$ is a typical layered-structure crystal with the I–Pb–I repeating units stacking along the *c*-axis and the van der Waals interlayer interaction,[24] which is often investigated and utilized as the precursor for the synthesis of CH$_3$NH$_3$PbI$_3$ (MAPbI$_3$) hybrid organic–inorganic 2D perovskite.[25–28] Until now, while most of the work is concentrated on their 2D morphologies with grain size on the order of tens of micrometers lying horizontally on

Dr. C. Lan, R. Dong, Z. Zhou, L. Shu, D. Li, S. P. Yip, Prof. J. C. Ho
Department of Materials Science and Engineering
City University of Hong Kong
Kowloon, Hong Kong S.A.R. 999077, P. R. China
E-mail: johnnyho@cityu.edu.hk

Dr. C. Lan
School of Optoelectronic Information
University of Electronic Science and Technology of China
Chengdu 610054, P. R. China

Z. Zhou, L. Shu, D. Li, S. P. Yip, Prof. J. C. Ho
Shenzhen Research Institute
City University of Hong Kong
Shenzhen 518057, P. R. China

L. Shu, S. P. Yip, Prof. J. C. Ho
State Key Laboratory of Millimeter Waves
City University of Hong Kong
Kowloon, Hong Kong S.A.R. 999077, P. R. China

Prof. J. C. Ho
Centre for Functional Photonics
City University of Hong Kong
Kowloon, Hong Kong S.A.R. 999077, P. R. China

The ORCID identification number(s) for the author(s) of this article can be found under https://doi.org/10.1002/adma.201702759.

**ADVANCED
SCIENCE NEWS**
www.advancedsciencenews.com

**ADVANCED
MATERIALS**
www.advmat.de

the substrate,[25–28] there are limited reports focusing on the large-scale synthesis and potential applications of freestanding PbI_2 and $MAPbI_3$ nanostructures.[29,30] In general, PbI_2 nanoplates or nanosheets can be synthesized by the solution method, where the charge state of the basic growth unit can be manipulated by suitable mineralizers to facilitate the 2D anisotropic growth of the crystals.[27,28,30] Also, various PbI_2 nanostructures, including nanowires, nanosheets, and atomically thin monolayers, can as well be realized by conventional physical vapor deposition (PVD) performed in a horizontal vacuum tube furnace.[31–33] Specifically, Liu et al. developed a combined solution/vapor-phase scheme to first obtain PbI_2 nanosheets by hot casting and then convert them into 2D $MAPbI_3$ nanocrystals as thin as a single unit cell down to 1.3 nm via chemical vapor deposition.[27] When configured into photodetectors, these 2D perovskites exhibit impressive photoelectric properties, displaying a photoresponsivity of 22 A W^{-1} with a voltage bias of 1 V under a 405 nm laser.[27] Combined with the complex device geometry and/or the hybrid material structure, the record-high performance of these 2D-$MAPbI_3$-based photodetectors can be further obtained.[34–36] Nevertheless, a majority of these studies was performed with the growth of small-scale PbI_2 or $MAPbI_3$ nanostructures heavily relying on the underlying substrates. To date, it is still a challenging task to achieve high-quality lead-halides as well as their 2D perovskites with a high growth yield in large-scale for the deployment of these materials in practical devices.

Here, we demonstrate the large-scale synthesis of freestanding PbI_2 and $MAPbI_3$ nanosheets on Si substrates with roughened surface via controlled growth kinetics in the PVD process. In contrast to the 2D growth on smooth substrates, the effect of process pressure and substrate surface can be manipulated to enable the formation of lead-halide nanosheets with high growth yield and excellent crystallinity. Notably, without adopting any sophisticated device and/or materials structures, the fabricated PbI_2 nanosheet can be configured into simple photoconductors, exhibiting impressive photosensing properties with a good responsivity of 410 mA W^{-1} at a wavelength of 405 nm, an excellent stability and an efficient time response (i.e., rise and decay time constants of 86 and 150 ms, respectively). When chemically transformed into $MAPbI_3$ materials, the photoresponsivity of these nanosheets is further improved to 40 A W^{-1}, which can be attributed to their intrinsically larger absorption coefficient as compared to PbI_2. All these results confirm evidently the technological potency of these highly crystalline freestanding nanosheets for high-performance photodetection.

As shown in the scanning electron microscopy (SEM) images in **Figure 1**a,b, during physical vapor deposition, when the process pressure is controlled to 4.5 Torr, high density of nanosheets can be readily obtained on the rough-surfaced substrate. It is obvious that these nanosheets are grown in a freestanding manner without relying on the underlying substrate, which is in a distinct contrast to the growth of 2D materials on smooth substrates.[33,37,38] Typically, these nanosheets have a flat and smooth surface morphology and a dimension of several tens of micrometers with a thickness in the range of 80–200 nm (Figure S1, Supporting Information). Also, the transmission electron microscopy (TEM) image shown in Figure 1c depicts the consistent results with the SEM characterization. Explicitly, the selected area electron diffraction (SAED) pattern displays the characteristic hexagonal symmetry of diffraction spots with the zone axis of [001], suggesting that the nanosheets are grown in the a–b plane with an excellent crystallinity. In order to verify the chemical composition and
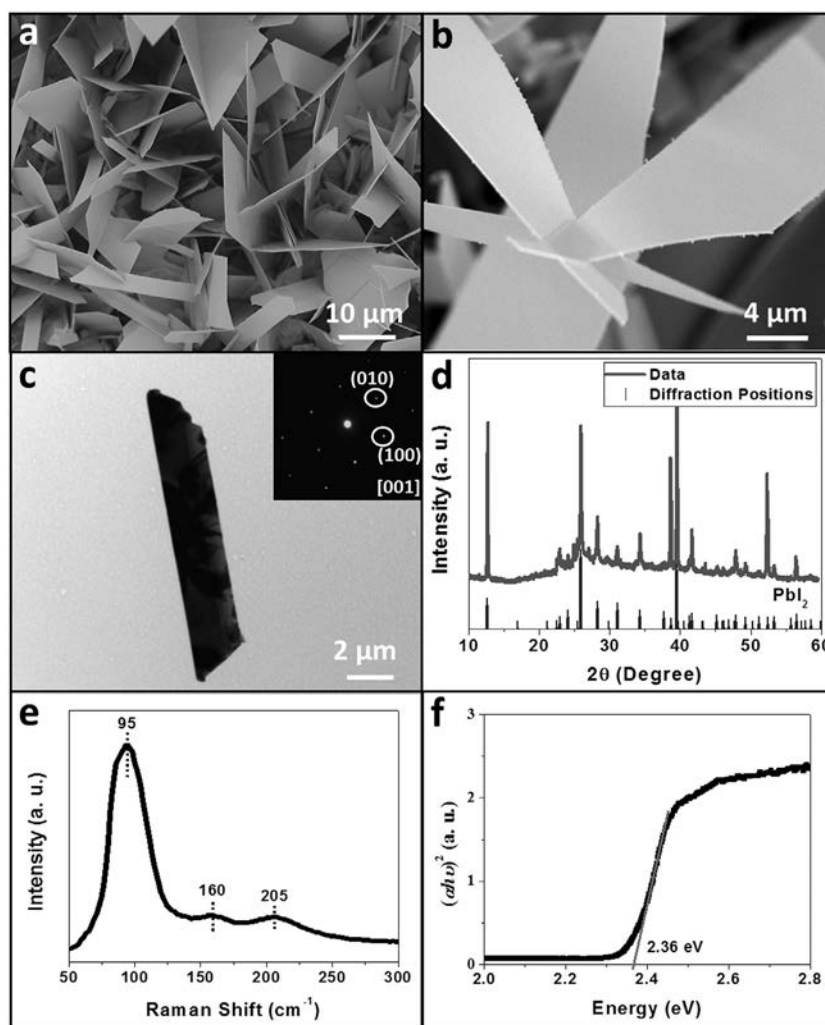

Figure 1. Characterization of as-synthesized PbI_2 nanosheets. a) Scanning electron microscopy (SEM) image. b) Zoom-in SEM image for the inspection of surface morphology. c) Transmission electron microscopy (TEM) image. The inset shows the corresponding selected area electron diffraction (SAED) pattern. d) X-ray diffraction (XRD) spectrum. e) Raman spectrum excited by a 532 nm laser. f) Tauc plot.

structural quality of these nanosheets, corresponding X-ray diffraction (XRD) spectrum was collected as shown in Figure 1d, where all the diffraction peaks can be clearly assigned to the hexagonal PbI_2 structure (JCPDS: 73-1752) without any other impurity phases, indicating the nanosheets being pure PbI_2 crystals. Raman spectroscopy and UV–vis absorption measurement were also performed on the PbI_2 nanosheets (Figure 1e,f). Three dominant Raman peaks are clearly observed at the location of 95, 160, and 205 cm^{-1}, corresponding to the A_{1g}, $2E_g$, and $4E_u$ of Raman modes of PbI_2, accordingly.[39] The Tauc plot reveals that the nanosheets have a direct bandgap of 2.36 eV. All these findings are in perfect agreement with the structure and properties of high-quality PbI_2 nanosheets and single crystals in the literature.[29,32] Because of the freestanding configuration, these high-density PbI_2 nanosheets can be beneficial as excellent channel materials for 2D devices.

In order understand the growth kinetics of these freestanding PbI_2 nanosheets, the effect of substrate surface morphology and process conditions are thoroughly investigated here. At first, Si substrates with the atomically flat surface are utilized to synthesize PbI_2 nanostructures in the PVD process. As shown in **Figure 2**a, large nanosheets lying flat on the substrate are attained instead of the freestanding nanostructures. It is noted that the modulation of other process parameters, such as the carrier gas flow rate, growth process and so on, only changes the dimension and thickness of nanosheets obtained, but does not modify their 2D morphology growing along the substrate surface (data shown later). However, after the surface irregularity has been deliberately introduced onto the Si substrate (roughened surfaces), the growth of PbI_2 nanostructures, especially their morphologies, becomes extremely sensitive to the growth pressure. When relatively low process pressure of 0.6 Torr is used, the highly dense and close-packed self-supporting nanosheet structure is achieved for the evolution of high-density freestanding PbI_2 nanosheets as illustrated in Figure 2b. With further increase in the pressure (e.g., 4.5 Torr), the density and dimension of nanosheets continued to decrease to yield a standalone nanosheet morphology (Figure 1a). When the process pressure was increased to above a certain threshold value (e.g., 200 Torr), the low-density PbI_2 nanowires can be produced on the substrate surface as given in Figure 2c. The existence of catalytic nanoparticle is also clearly observed at the tip region of the nanowire, which reveals that the nanowire grows via the vapor–liquid–solid (VLS) or vapor–solid–solid mechanism there (Figure 2c inset). Evidently, the growth morphology of these PbI_2 nanostructures can be effectively modulated by varying the substrate roughness as well as the process pressure taken place in the PVD system.

To shed light on the growth mechanisms of different PbI_2 nanostructures obtained under varied process conditions, an understanding of the crystal structure of 2D layered PbI_2 materials would be helpful. As demonstrated in **Figure 3**a inset, PbI_2 has a layered structure with the in-plane a–b lattice plane and the layers are stacked along the c-axis. Usually, the crystal plane with the highest atomic packing density would have the lowest amount of dangling bonds, and hence the lowest surface energy. In this case, the highest packing plane of PbI_2 is (001), which has the lowest surface energy.[33] At the same time, during the crystal growth, nucleation would preferentially
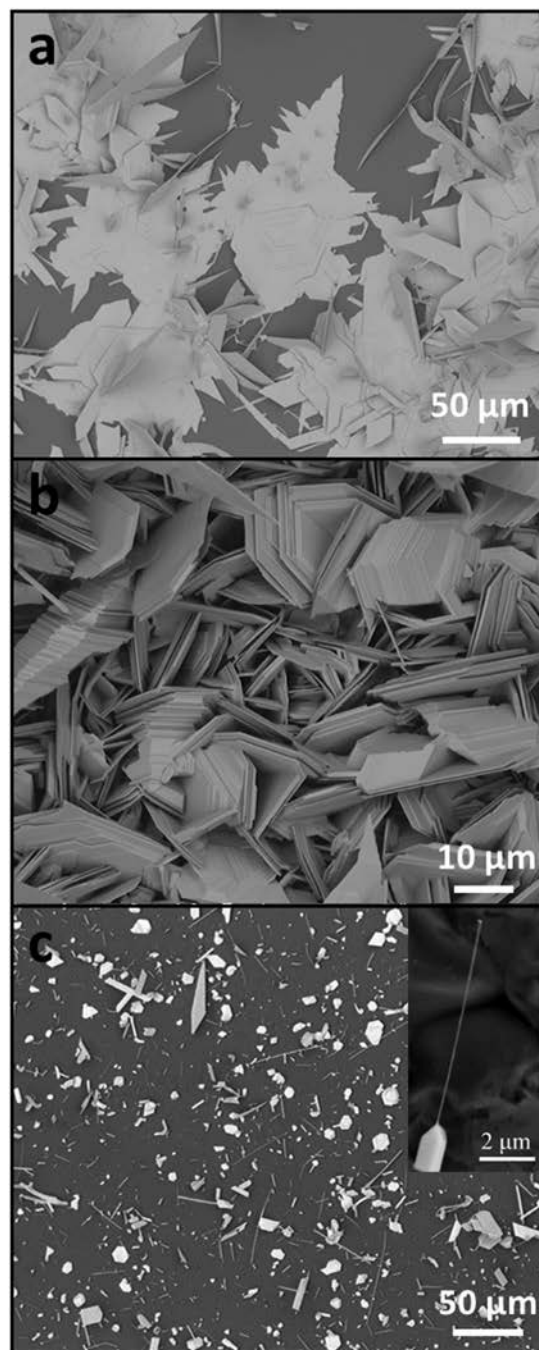

Figure 2. Various PbI_2 nanostructures obtained at different process conditions. a) Large nanosheets lying flat on a smooth Si surface with the process pressure of 4.5 Torr. b) High density of freestanding nanosheets on a roughened Si surface with the process pressure of 0.6 Torr. c) Low-density of nanowire on a roughened Si surface with the process pressure of 200 Torr. The inset shows the corresponding high-magnification image depicting the nanowire morphology obtained.

occur in this low energy surface plane of (001); therefore, the nuclei with layered crystal planes (i.e., a–b planes) are predominantly initiated parallel to the underlying substrate surface. As the nucleation progresses, the new coming PbI_2 species and/or their constituents would get adsorbed on the PbI_2 nuclei as

**ADVANCED
SCIENCE NEWS**
www.advancedsciencenews.com
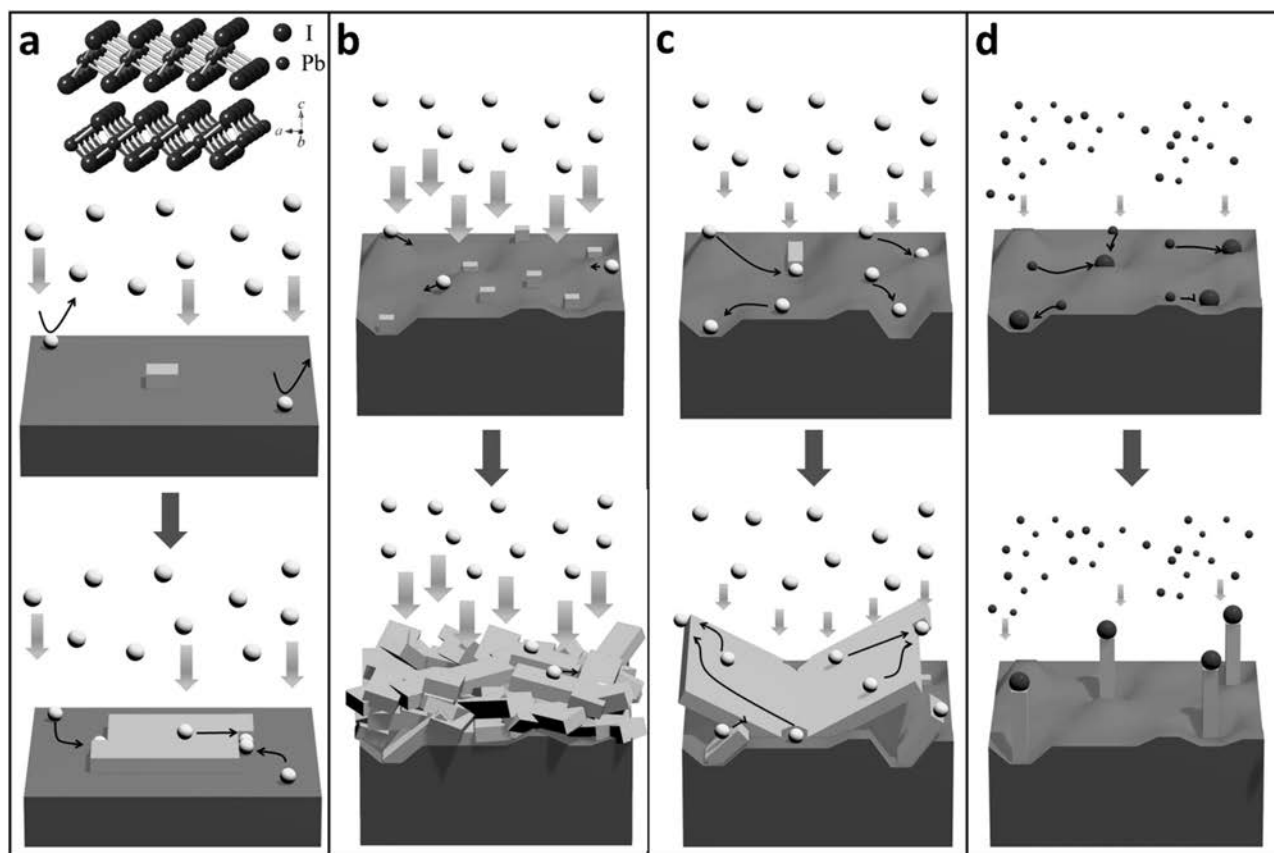
**ADVANCED
MATERIALS**
www.advmat.de

Figure 3. Schematic illustration of the growth kinetics and mechanisms of various PbI$_2$ nanostructures obtained with different substrate and process conditions. a) Growth behavior of 2D nanosheets lying flat onto the smooth Si substrate. Inset shows the atomic model of PbI$_2$, depicting its layered structure and repeating I–Pb–I unit cells stacked along the c-axis. b) Formation of highly dense and close-packed self-supporting nanosheets taken place on the rough-surfaced substrate with the relatively low process pressure. c) Formation of less dense and freestanding nanosheets taken place on the rough-surfaced substrate with the increased process pressure. d) Growth of nanowires resulted on the rough-surfaced substrate with the highest process pressure.

well as on the substrate surface and then be migrated to the growth sites. Due to the weak van der Waals interaction in the out-of-plane direction with adsorbed species and strong covalent interaction with adsorbed species in the lateral direction, the growth sites of layered PbI$_2$ are always located at the edges as illustrated in Figure 3a, similar to other types of layered materials.[38] If the substrate surface is smooth, the PbI$_2$ nuclei would then be expanded in the in-plane direction and grown into a large sheet-like structure. In fact, the phenomenon is more obvious when the atomically smooth mica substrate is employed, in which no dangling bonds exist at the surface so that the PbI$_2$ nanosheets are observed to grow via the typical epitaxial 2D material growth along the substrate surface there (Figure S2a,c, Supporting Information).[26] On the other hand, if a rough substrate is utilized in the growth, since there are a lot of microplanes with different angles relative to the in-plane direction of the substrate as shown in Figure 3b, the expansion or further growth of the nuclei would occur in limited directions and result in the freestanding PbI$_2$ nanosheets. More importantly, when the process or deposition pressure is low, the evaporation of PbI$_2$ source becomes fast, leading to the fast feeding of PbI$_2$ species at the deposition location and thus inducing an increased out-of-plane growth for the formation of

high-density close-packed nanosheets. Further increase in the pressure would slow down the feeding of the precursor so that the density and dimension of synthesized nanosheets decrease accordingly (Figure 3c). When the deposition pressure becomes extremely high, the evaporated PbI$_2$ would mostly disassociate into elemental or molecular Pb and I species. As I has a relatively low boiling point of 185.2 °C,[40] it cannot form liquid droplets at the growth temperature. Pb has a higher boiling point of 1749 °C, but a low melting point of 327.4 °C;[40] therefore, it is possible for Pb species to aggregate into Pb liquid droplets during the growth. This way, the Pb droplets can function as the catalytic tips absorbing PbI$_2$ species or their constituents. The PbI$_2$ nanowires can then be grown after the catalytic supersaturation of PbI$_2$ in the Pb liquid droplets via VLS mechanism. In the cooling process of the growth, the Pb liquid droplets can also react with the I species, forming PbI$_2$ nanoparticles at the tip region of the PbI$_2$ nanowires as demonstrated in Figure 3d. In any case, the rough substrate surface is essential for the growth of PbI$_2$ nanowires as it can provide a microenvironment with an absence of I species due to their volatility and their slow feeding, which is beneficial for the formation of Pb droplets. If the smooth substrate is used instead, no nanowires can be found (Figure S2b,c, Supporting Information). All these
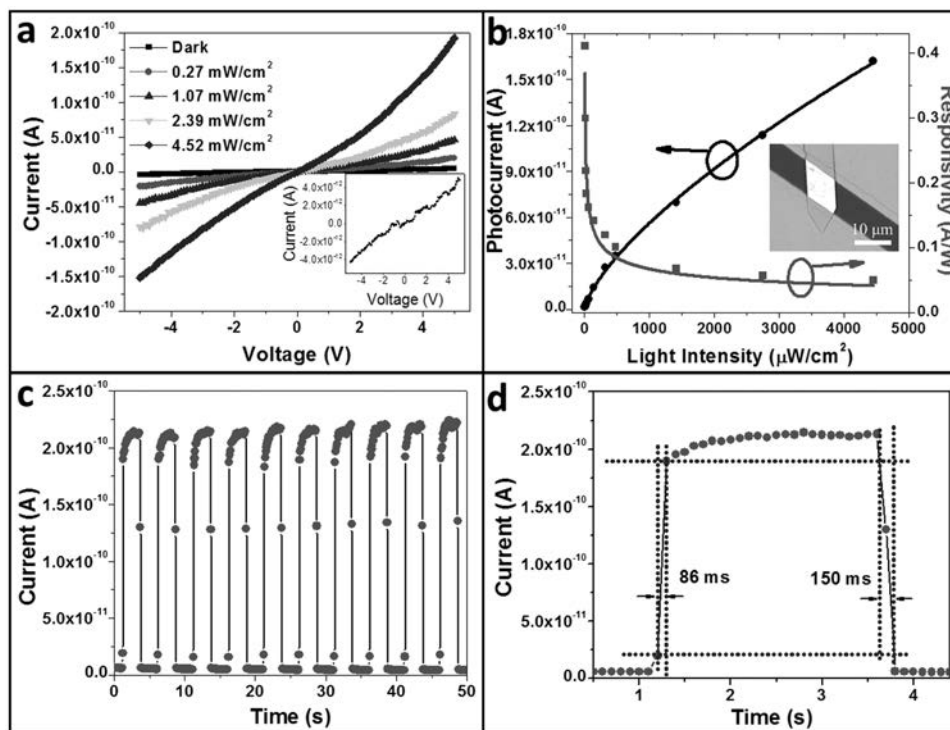
Figure 4. Photoresponse of PbI$_2$ nanosheet photodetectors. a) I–V curves without and with the light illumination. Inset: I–V curve in the dark state. b) Photocurrent and responsivity as a function of incident light intensity. Inset gives the SEM image of the device. c) The device output current as a function of time under the chopped light illumination. The light intensity is 4.66 mW cm^{-2}. d) A high-resolution part of (c) to show the rise time and decay time constants. The bias voltage for (b)–(d) is 5 V.

findings suggest and further confirm the importance of various microenvironment required for the formation of different PbI$_2$ nanostructures, including flat lying, freestanding nanosheets and nanowires.

Apart from understanding the growth kinetics and mechanisms, since multilayer PbI$_2$ is a direct bandgap semiconductor, it is interesting to assess the optoelectronic properties of our PbI$_2$ nanosheets. In this case, photodetectors made of freestanding PbI$_2$ nanosheet is fabricated and electrically characterized under illumination (**Figure 4**b inset). The close-to-linear relation of the current *versus* the bias voltage (I–V) in the dark (Figure 4a inset) qualitatively suggests the existence of only a relatively small potential barrier between the nanosheet and the electrodes, which is beneficial for the collection of photogenerated carriers. Note that this rather effective electrical contact is important for the subsequent device performance assessment. The structure is then illuminated with a 405 nm source with different intensity. As shown in Figure 4a, when the illumination intensity is increased, the device output current increases accordingly. This enhanced output current has a typical linear relationship with the bias voltage, indicating that a large bias voltage can induce a large photocurrent (defined as the difference of current with and without the light illumination). In order to better understand the photosensing behavior of the PbI$_2$ nanosheet photodetector, the dependence of its photocurrent on different light intensities is measured and depicted in Figure 4b. The measured data can be well fitted by Equation (1):

$$I_p = A\Phi^\beta \tag{1}$$

where I_p is the photocurrent, A and β are the fitting parameters, and Φ is the light intensity. The parameter of β is determined as 0.7 from the fitting of the measured data, revealing the sublinear relationship between the photocurrent and light intensity, which is often observed in layered-material-based photoconductors[18,37,41,42] due to the complex processes of electron–hole generation, trapping, and recombination in the semiconductors.[18,43,44] Regardless, two important figure of merits, responsivity (R) and detectivity (D^*), are always employed to evaluate the characteristics of photodetectors, which are defined as:

$$R = \frac{I_p}{\Phi S} \tag{2}$$

$$D^* = R \cdot \sqrt{\frac{S}{2eI_d}} \tag{3}$$

where S is the active area of the photodetector, e is the absolute value of the charge of an electron, and I_d is the dark current. As can be seen, D^* is proportional to R and hence, D^* has the same variation trend with R. As demonstrated in Figure 4b, R is observed to be a decreasing function of the light intensity due to the sublinear relation between photocurrent and light intensity according to Equation (1) and (2), all these would lead to the relation of $R \propto \Phi^{\beta-1}$ or $R \propto \Phi^{-0.3}$. The maximum R and corresponding D^* are found to be 410 mA V^{-1} and 3.1×10^{11} Jones across the entire measured range.

The repeatability and response speed are another two essential parameters for the performance assessment of photodetectors. The repeatability can be appraised by measuring the photocurrent as a function of time (i.e., I–t curves) under chopped illumination in Figure 4c. It is obvious that the device on- and off-state can be effectively modulated by the chopped illumination with a good repeatability and a decent on/off current ratio of 42. A high-resolution I–t curve is then utilized to study the response speed of the photodetector. Usually, the time needed for the current to increase from 10% to 90% of the peak value and vice versa are defined as the rise time and decay time constants, respectively. Based on the measurement presented in Figure 4d, the rise and decay time constants can be identified as 86 and 150 ms, accordingly. The sharp rise followed by the slow rise is often observed in photodetectors based on nanomaterials, in which this switching nature can be attributed to the traps and defect states in the bulk or on the material surface.[45–47] In specific, the photogenerated carriers would first fill the traps and then the photocurrent would reach the maximum after all traps are occupied, which brings a deferral in getting the steady photocurrent.[45] For comparison, the freestanding PbI$_2$ nanowires are also configured into the similar photodetector structures and characterized accordingly (Figure S3, Supporting Information). The photoresponsivity of PbI$_2$ nanowire detectors is found to be lot smaller than that of PbI$_2$ nanosheet photodetectors, which can be attributed to the anisotropic light absorption and polarization-sensitive photodetection of 1D nanowire materials. Regardless, all these obtained performance indicators of nanosheet detectors are highly comparable or even better than those of state-of-the-art PbI$_2$ and other layered nanostructured materials as reported in the recent literature (**Table 1**),[30,31,48] illustrating the impressive performance and promising prospect of our freestanding PbI$_2$ nanosheets for the highly efficient photodetection.

As mentioned earlier, PbI$_2$ is often employed as the precursor to synthesize MAPbI$_3$, which has been demonstrated to exhibit many astonishing optoelectronic properties.[26,49,50] In this work, we also revealed that the as-prepared PbI$_2$ nanosheets can be converted into MAPbI$_3$ nanosheets by the chemical vapor deposition (CVD) method.[26,51] As shown in the SEM images in **Figure 5**a, after the conversion, the freestanding nanosheet morphology is retained except for the roughening surface. It is noted that the MAPbI$_3$ nanosheets become slightly thicker than the ones of PbI$_2$ (Figure S4, Supporting Information), which is anticipated to be caused by the insertion of organic species into the PbI$_2$ crystal lattice. The dark contrast of the corresponding TEM image (Figure 5b) as well indicates that the nanosheet is relatively thick, being consistent to the SEM results. XRD performed on these MAPbI$_3$ nanosheets confirms the complete conversion of PbI$_2$ into MAPbI$_3$ as illustrated in Figure 5c.[52,53] However, based on the Raman spectrum of MAPbI$_3$ collected in Figure S5 in the Supporting Information, it seems that the MAPbI$_3$ nanosheets partially degraded due to the instability of MAPbI$_3$ materials in ambient.[54,55] Although the MAPbI$_3$ nanosheets are partially degraded, they still exhibit an impressively strong photoluminescence (PL) with the emission peak located at 1.58 eV, which is in perfect agreement with the bandgap of 1.54 eV determined from the Tauc plot as depicted in Figure 5d. Because of this direct bandgap with the extraordinarily high optical absorption, it is interesting to assess the optoelectronic properties, especially the photosensing performance, of synthesized MAPbI$_3$ nanosheets. Photodetectors based on MAPbI$_3$ nanosheet were fabricated (Figure 5f inset) and their performance was measured. It is obvious that the effective on/off switching can be achieved in the I–t curve under chopped illumination (Figure 5e). The on/off current ratio is found to be 400, which is much larger than that of PbI$_2$ nanosheets. The rise and decay time constants can also be determined from Figure 5f, which is 1.4 s and 90 ms, respectively. Importantly, the responsively under a light intensity of 1.27 mW cm^{-2} is measured to be 40 A W^{-1}, much larger than that of PbI$_2$ under the same light intensity (about 0.07 A W^{-1}). This enhanced photoresponsivity can be partly attributed to their larger optical absorption coefficient[56] as well as their increased sheet thickness of MAPbI$_3$ nanosheets as compared with those of PbI$_2$ nanosheets, which lead to the enhanced light absorption (see Figure S6, Supporting Information). Also, the intrinsic properties of MAPbI$_3$, such as high electrical mobility,[57] long range balanced electron and hole lengths,[58,59] may also lead to the enhanced photoresponsivity.

Table 1. Comparison of various figure of merits of different representative layered-material-based photodetectors.

| Material	Light	Bias	Dark current	Responsivity	Detectivity	Rise time	Decay time	Reference
PbI$_2$ nanosheet	405 nm	5 V	5.1 pA	410 mA W^{-1}	3.1×10^{11} Jones	86 ms	150 ms	This work
PbI$_2$ nanoplate	450 nm	1.9 V	10 fA	0.1 mA W^{-1}	–	55 µs	110 µs	[30]
PbI$_2$ nanowire	450 nm	3 V	1.8 pA	100 mA W^{-1}	–	0.79 s	0.91 s	[31]
PbI$_2$ nanoplate	450 nm	5 V	10 pA	147.6 A W^{-1}	2.56×10^{11} Jones	18 ms	23 ms	[29]
PbI$_2$ single crystal	440 nm	15 V	1.38 nA	11.3 A W^{-1}	–	–	354 µs	[32]
GaTe nanosheet	473 nm	5 V	0.38 nA	30 mA W^{-1}	–	54 ms	54 ms	[60]
Multilayer WS$_2$	514 nm	5 V	–	92 µA W^{-1}	–	5.3 ms	5.3 ms	[61]
Bi$_2$S$_3$ nanosheet	632.8 nm	0.5 V	0.2 µA	4.4 A W^{-1}	2.1×10^{11} Jones	10 µs	350 µs	[62]
Monolayer MoSe$_2$	532 nm	10 V	0.18 nA	13 mA W^{-1}	–	60 ms	60 ms	[63]
Monolayer MoS$_2$	561 nm	8 V (gate bias of −70 V)	2 pA	880 A W^{-1}	–	4 s	9 s	[18]
TiS$_3$ nanoribbon	640 nm	1 V (gate bias of −40 V)	–	2910 A W^{-1}	–	4 ms	9 ms	[64]
Few-layer ReS$_2$	532 nm	4 V (gate bias of −50 V)	–	88 600 A W^{-1}	–	1–100 s	1–100 s	[65]
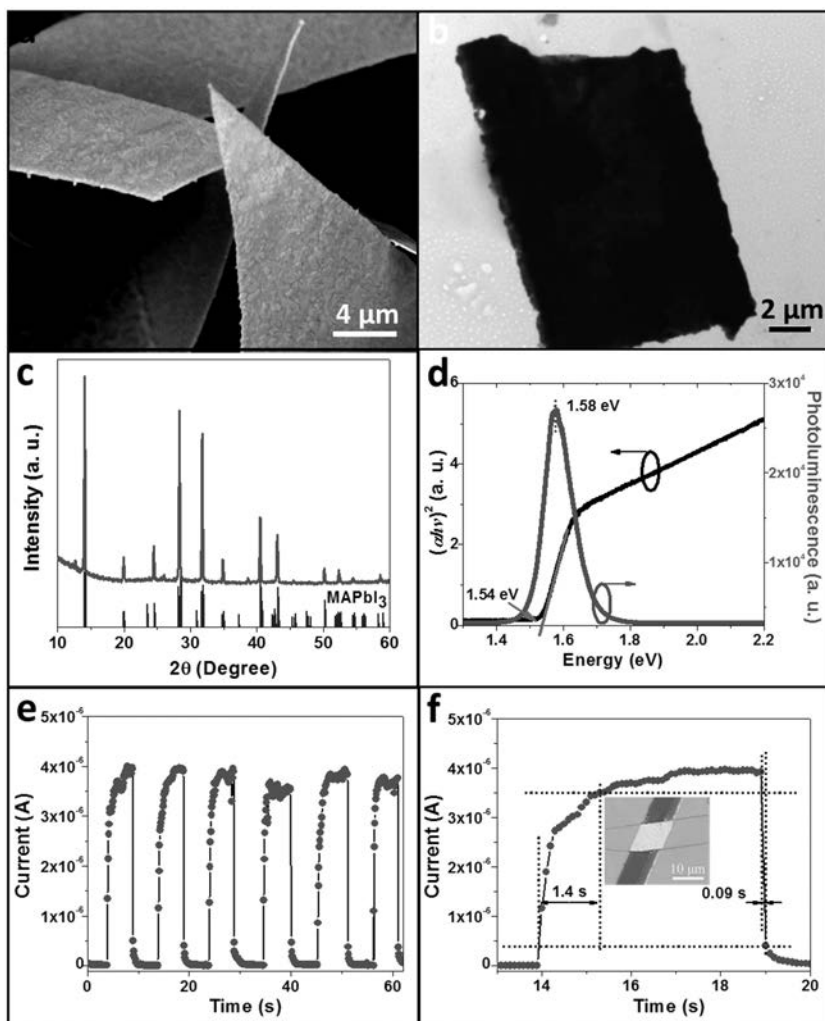
Figure 5. Characterization and optoelectronic properties of as-synthesized MAPbI$_3$ nanosheets. a) XRD spectrum. b) High-resolution SEM image. c) TEM image. d) Tauc plot and photoluminescence spectrum (excited by a 532 nm laser). e) The device output current as a function of time under chopped light illumination. The light intensity is 1.27 mW cm^{-2} and the bias voltage is 5 V. f) A high-resolution part of (e) to show the rise time and decay time constants. The inset shows an SEM image of the device.

All these results indicate clearly the excellent photoelectric properties of our freestanding MAPbI$_3$ nanosheets for high-performance photodetector applications. More detailed studies aiming at establishing appropriate passivation schemes to further enhance the stability of MAPbI$_3$ nanosheets are underway.

In conclusion, large-scale synthesis of various PbI$_2$ nanostructures, including nanosheets, nanowires, etc., is successfully demonstrated with the manipulation of different substrate surface morphology and growth pressure employed in the PVD process. Specifically, utilizing intentionally roughened Si substrate surfaces with the optimal process pressure, highly crystalline, high-density and freestanding PbI$_2$ nanosheets can be readily obtained. When configured into photodetectors, these nanosheets exhibit an impressive responsivity of 410 mA W^{-1}, and a fast response with the rise and decay time constants of 86 and 150 ms, respectively, under an illumination wavelength of 405 nm. Furthermore, these PbI$_2$ nanosheets can be completely

converted into MAPbI$_3$ nanosheets, which display a much improved photoresponsivity when fabricated into photodetectors. All these performance parameters are comparable or even superior to the ones fabricated with state-of-the-art layered materials, highlighting the technological potency of our freestanding PbI$_2$ and MAPbI$_3$ nanosheets for various practical utilization in optoelectronics.

Experimental Section

Synthesis of PbI$_2$ Nanosheets: In this study, the PbI$_2$ nanostructures were synthesized by physical vapor deposition. In detail, the solid powder of PbI$_2$ (50 mg and 99% purity) was used as the source material, which was loaded in a quartz boat. Then, the quartz boat was inserted into the center of a quartz tube that was mounted into a horizontal tube furnace. At the same time, prime-grade Si pieces (boron doped, 0.001–0.005 Ω cm resistivity) with both smooth and rough surfaces were utilized as the growth substrates. The smooth Si was employed directly as received from the vendor after it was thorough cleaned with deionized water, acetone, and ethanol for 5 min each under ultrasonication sequentially and blow-dry with nitrogen. The rough Si was prepared by a gentle polishing with 1000 mesh sand paper for 5 min, followed by the same thorough cleaning procedures and blow-dry with nitrogen. During the growth, the substrate was placed in the downstream side of the quartz tube, which was 13 cm away from the source powder, and the entire system was pumped down to a base pressure of 1.2 mTorr and maintained for 30 min. Next, the high-purity Ar gas (99.999%) was injected into the system with controlled flow rate (e.g., 50 sccm) to generate different process pressure (e.g., 4.5 Torr). After that, the furnace was heated to 400 °C in 12 min for the growth of PbI$_2$ nanostructures, and then it was cooled down to room temperature naturally with the gas flow maintained. Eventually, a layer of the orange yellow product could be collected on the substrate.

Synthesis of MAPbI$_3$ Nanosheets: For the conversion of PbI$_2$ into MAPbI$_3$ materials, the source powder of methylammonium iodide (CH$_3$NH$_3$I, 50 mg, 98% purity) was loaded in a ceramic boat and placed into the center of a quartz tube. The substrate with as-grown PbI$_2$ nanosheets was then positioned in the downstream side of the quartz tube, which was again 13 cm away from the source powder, and the quartz tube was mounted on a horizontal tube furnace. High-purity Ar gas (99.999%) was utilized as the carrier gas while its flow rate was kept at 100 sccm. During the material conversion, the process pressure was maintained at 50 Torr. The furnace was then heated to 130 °C in 12 min and kept at that temperature for the duration of 5 h. After that, the orange yellow product would turn into black color on the substrate.

Material Characterization: XRD (D2 Phaser, Bruker) was used to evaluate the crystallinity and crystal structure of the products. The morphologies of the products were then studied by SEM (G2 Pro, PhenomWorld) and TEM (CM20, Philips). The crystallinity of the products was as well verified by SAED attached in TEM. Raman and PL spectra were measured by a Raman spectrometer (SR-5001-A-R, Andor) with a 532 nm laser. Corresponding reflectance spectra (*r*) were also measured using UV–vis spectrometer (Lambda 750, PerkinElmer),

**ADVANCED
SCIENCE NEWS**

www.advancedsciencenews.com

**ADVANCED
MATERIALS**

www.advmat.de

which were converted to absorbance spectra ($\alpha = -B\ln(r)$, where B is a film thickness related coefficient).

Nanosheet Device Fabrication and Electrical Characterization: For the device fabrication, the nanosheets were first transferred onto the degenerately doped p-type Si substrates with a 270 nm thick thermally grown gate oxide layer using a physical dry transfer technique. Nickel grid was next used as the shadow mask and attached onto the substrate. Ti (5 nm) and Au (100 nm) thin films were deposited via thermal evaporation as the electrical contact electrode. The devices were baked at 100 °C for 10 min to aim for effective electrical contact between the sheet and the electrodes. The electrical performance of the fabricated device was then characterized with a standard electrical probe station and an Agilent 4155C semiconductor analyzer (Agilent Technologies, California, USA). A 405 nm laser diode was used as light source for the photodetection measurement, while the power of the incident irradiation was measured using a power meter (PM400, Thorlabs). An attenuator was also employed to tune the irradiation power that was illuminated on the device.

Supporting Information

Supporting Information is available from the Wiley Online Library or from the author.

Conflict of Interest

The authors declare no conflict of interest.

[1] K. F. Mak, J. Shan, *Nat. Photonics* **2016**, *10*, 216.
[2] K. Novoselov, A. Mishchenko, A. Carvalho, A. C. Neto, *Science* **2016**, *353*, 461.
[3] G. R. Bhimanapati, Z. Lin, V. Meunier, Y. Jung, J. Cha, S. Das, D. Xiao, Y. Son, M. S. Strano, V. R. Cooper, *ACS Nano* **2015**, *9*, 11509.
[4] L. Cao, *MRS Bull.* **2015**, *40*, 592.
[5] J. S. Ponraj, Z.-Q. Xu, S. C. Dhanabalan, H. Mu, Y. Wang, J. Yuan, P. Li, S. Thakur, M. Ashrafi, K. Mccoubrey, *Nanotechnology* **2016**, *27*, 462001.
[6] M. J. Allen, V. C. Tung, R. B. Kaner, *Chem. Rev.* **2010**, *110*, 132.
[7] A. C. Ferrari, F. Bonaccorso, V. Fal'Ko, K. S. Novoselov, S. Roche, P. Bøggild, S. Borini, F. H. Koppens, V. Palermo, N. Pugno, *Nanoscale* **2015**, *7*, 4598.

[8] M. Li, D. Liu, D. Wei, X. Song, D. Wei, A. T. S. Wee, *Adv. Sci.* **2016**, *3*, 1600003.
[9] F. Xia, H. Wang, D. Xiao, M. Dubey, A. Ramasubramaniam, *Nat. Photonics* **2014**, *8*, 899.
[10] D. Jariwala, V. K. Sangwan, L. J. Lauhon, T. J. Marks, M. C. Hersam, *ACS Nano* **2014**, *8*, 1102.
[11] C. Xie, C. Mak, X. Tao, F. Yan, *Adv. Funct. Mater.* **2017**, *27*, 1603886.
[12] Q. H. Wang, K. Kalantar-Zadeh, A. Kis, J. N. Coleman, M. S. Strano, *Nat. Nanotechnol.* **2012**, *7*, 699.
[13] H. Liu, Y. Du, Y. Deng, D. Y. Peide, *Chem. Soc. Rev.* **2015**, *44*, 2732.
[14] D. Kong, W. Dang, J. J. Cha, H. Li, S. Meister, H. Peng, Z. Liu, Y. Cui, *Nano Lett.* **2010**, *10*, 2245.
[15] J. Shim, H. Y. Park, D. H. Kang, J. O. Kim, S. H. Jo, Y. Park, J. H. Park, *Adv. Electron. Mater.* **2017**, *3*, 1600364.
[16] A. Pant, Z. Mutlu, D. Wickramaratne, H. Cai, R. K. Lake, C. Ozkan, S. Tongay, *Nanoscale* **2016**, *8*, 3870.
[17] X. Zhou, Q. Zhang, L. Gan, H. Li, J. Xiong, T. Zhai, *Adv. Sci.* **2016**, *3*, 1600177.
[18] O. Lopez-Sanchez, D. Lembke, M. Kayci, A. Radenovic, A. Kis, *Nat. Nanotechnol.* **2013**, *8*, 497.
[19] L. Dou, A. B. Wong, Y. Yu, M. Lai, N. Kornienko, S. W. Eaton, A. Fu, C. G. Bischak, J. Ma, T. Ding, *Science* **2015**, *349*, 1518.
[20] Z. Guo, X. Wu, T. Zhu, X. Zhu, L. Huang, *ACS Nano* **2016**, *10*, 9992.
[21] D. Liang, Y. Peng, Y. Fu, M. J. Shearer, J. Zhang, J. Zhai, Y. Zhang, R. J. Hamers, T. L. Andrew, S. Jin, *ACS Nano* **2016**, *10*, 6897.
[22] Z. Tan, Y. Wu, H. Hong, J. Yin, J. Zhang, L. Lin, M. Wang, X. Sun, L. Sun, Y. Huang, *J. Am. Chem. Soc.* **2016**, *138*, 16612.
[23] J. Zhou, Y. Chu, J. Huang, *ACS Appl. Mater. Interfaces* **2016**, *8*, 25660.
[24] V. Agrawal, G. Chadha, G. Trigunayat, *Acta Crystallogr., Sect. A* **1970**, *26*, 140.
[25] H.-C. Cheng, G. Wang, D. Li, Q. He, A. Yin, Y. Liu, H. Wu, M. Ding, Y. Huang, X. Duan, *Nano Lett.* **2015**, *16*, 367.
[26] S. T. Ha, X. Liu, Q. Zhang, D. Giovanni, T. C. Sum, Q. Xiong, *Adv. Opt. Mater.* **2014**, *2*, 838.
[27] J. Liu, Y. Xue, Z. Wang, Z.-Q. Xu, C. Zheng, B. Weber, J. Song, Y. Wang, Y. Lu, Y. Zhang, *ACS Nano* **2016**, *10*, 3536.
[28] G. Wang, D. Li, H.-C. Cheng, Y. Li, C.-Y. Chen, A. Yin, Z. Zhao, Z. Lin, H. Wu, Q. He, *Sci. Adv.* **2015**, *1*, e1500613.
[29] M. Zhong, L. Huang, H.-X. Deng, X. Wang, B. Li, Z. Wei, J. Li, *J. Mater. Chem. C* **2016**, *4*, 6492.
[30] W. Zheng, Z. Zhang, R. Lin, K. Xu, J. He, F. Huang, *Adv. Electron. Mater.* **2016**, *2*, 1600291.
[31] J. Liu, Z. Liang, B. Xu, H. Xiang, Y. Xia, J. Yin, Z. Liu, *RSC Adv.* **2016**, *6*, 59445.
[32] J. Zhang, T. Song, Z. Zhang, K. Ding, F. Huang, B. Sun, *J. Mater. Chem. C* **2015**, *3*, 4402.
[33] M. Zhong, S. Zhang, L. Huang, J. You, Z. Wei, X. Liu, J. Li, *Nanoscale* **2017**, *9*, 3736.
[34] P.-H. Chang, S.-Y. Liu, Y.-B. Lan, Y.-C. Tsai, X.-Q. You, C.-S. Li, K.-Y. Huang, A.-S. Chou, T.-C. Cheng, J.-K. Wang, *Sci. Rep.* **2017**, *7*, 46281.
[35] H. Wang, R. Haroldson, B. Balachandran, A. Zakhidov, S. Sohal, J. Y. Chan, A. Zakhidov, W. Hu, *ACS Nano* **2016**, *10*, 10921.
[36] L. Su, Z. X. Zhao, H. Y. Li, J. Yuan, Z. L. Wang, G. Z. Cao, G. Zhu, *ACS Nano* **2015**, *9*, 11310.
[37] C. Lan, C. Li, Y. Yin, Y. Liu, *Nanoscale* **2015**, *7*, 5974.
[38] L. Huang, Y. Yu, C. Li, L. Cao, *J. Phys. Chem. C* **2013**, *117*, 6469.
[39] W. M. Sears, M. Klein, J. Morrison, *Phys. Rev. B* **1979**, *19*, 2305.
[40] *Lange's Handbook of Chemistry*, 15th ed., (Ed: J. A. Dean), McGraw-Hill, New York **1999**.
[41] C. Lan, C. Li, S. Wang, T. He, Z. Zhou, D. Wei, H. Guo, H. Yang, Y. Liu, *J. Mater. Chem. C* **2017**, *5*, 1494.
[42] C. Lan, C. Li, Y. Yin, H. Guo, S. Wang, *J. Mater. Chem. C* **2015**, *3*, 8074.

[43] F. Binet, J. Duboz, E. Rosencher, F. Scholz, V. Härle, *Appl. Phys. Lett.* **1996**, *69*, 1202.

[44] C. Soci, A. Zhang, B. Xiang, S. A. Dayeh, D. Aplin, J. Park, X. Bao, Y.-H. Lo, D. Wang, *Nano Lett.* **2007**, *7*, 1003.

[45] Y. Jiang, W. J. Zhang, J. S. Jie, X. M. Meng, X. Fan, S. T. Lee, *Adv. Funct. Mater.* **2007**, *17*, 1795.

[46] G. Cunningham, U. Khan, C. Backes, D. Hanlon, D. McCloskey, J. F. Donegan, J. N. Coleman, *J. Mater. Chem. C* **2013**, *1*, 6899.

[47] X. Zhou, Q. Zhang, L. Gan, H. Li, T. Zhai, *Adv. Funct. Mater.* **2016**, *26*, 4405.

[48] M. Buscema, J. O. Island, D. J. Groenendijk, S. I. Blanter, G. A. Steele, H. S. van der Zant, A. Castellanos-Gomez, *Chem. Soc. Rev.* **2015**, *44*, 3691.

[49] L. Gu, M. M. Tavakoli, D. Zhang, Q. Zhang, A. Waleed, Y. Xiao, K. H. Tsui, Y. Lin, L. Liao, J. Wang, *Adv. Mater.* **2016**, *28*, 9713.

[50] F. Li, C. Ma, H. Wang, W. Hu, W. Yu, A. D. Sheikh, T. Wu, *Nat. Commun.* **2015**, *6*, 8238.

[51] J. Xing, X. F. Liu, Q. Zhang, S. T. Ha, Y. W. Yuan, C. Shen, T. C. Sum, Q. Xiong, *Nano Lett.* **2015**, *15*, 4571.

[52] T. Baikie, Y. Fang, J. M. Kadro, M. Schreyer, F. Wei, S. G. Mhaisalkar, M. Graetzel, T. J. White, *J. Mater. Chem. A* **2013**, *1*, 5628.

[53] Y. Dang, Y. Liu, Y. Sun, D. Yuan, X. Liu, W. Lu, G. Liu, H. Xia, X. Tao, *CrystEngComm* **2015**, *17*, 665.

[54] M. Ledinský, P. Löper, B. Niesen, J. Holovský, S.-J. Moon, J.-H. Yum, S. De Wolf, A. Fejfar, C. Ballif, *J. Phys. Chem. Lett.* **2015**, *6*, 401.

[55] P. Pistor, A. Ruiz, A. Cabot, V. Izquierdo-Roca, *Sci. Rep.* **2016**, *6*, 35973.

[56] S. De Wolf, J. Holovsky, S.-J. Moon, P. Löper, B. Niesen, M. Ledinsky, F.-J. Haug, J.-H. Yum, C. Ballif, *J. Phys. Chem. Lett.* **2014**, *5*, 1035.

[57] C. C. Stoumpos, C. D. Malliakas, M. G. Kanatzidis, *Inorg. Chem.* **2013**, *52*, 9019.

[58] S. D. Stranks, G. E. Eperon, G. Grancini, C. Menelaou, M. J. Alcocer, T. Leijtens, L. M. Herz, A. Petrozza, H. J. Snaith, *Science* **2013**, *342*, 341.

[59] G. Xing, N. Mathews, S. Sun, S. S. Lim, Y. M. Lam, M. Grätzel, S. Mhaisalkar, T. C. Sum, *Science* **2013**, *342*, 344.

[60] Z. Wang, M. Safdar, M. Mirza, K. Xu, Q. Wang, Y. Huang, F. Wang, X. Zhan, J. He, *Nanoscale* **2015**, *7*, 7252.

[61] N. Perea-López, A. L. Elías, A. Berkdemir, A. Castro-Beltran, H. R. Gutiérrez, S. Feng, R. Lv, T. Hayashi, F. López-Urías, S. Ghosh, *Adv. Funct. Mater.* **2013**, *23*, 5511.

[62] G. Chen, Y. Yu, K. Zheng, T. Ding, W. Wang, Y. Jiang, Q. Yang, *Small* **2015**, *11*, 2848.

[63] J. Xia, X. Huang, L.-Z. Liu, M. Wang, L. Wang, B. Huang, D.-D. Zhu, J.-J. Li, C.-Z. Gu, X.-M. Meng, *Nanoscale* **2014**, *6*, 8949.

[64] J. O. Island, M. Buscema, M. Barawi, J. M. Clamagirand, J. R. Ares, C. Sánchez, I. J. Ferrer, G. A. Steele, H. S. van der Zant, A. Castellanos-Gomez, *Adv. Opt. Mater.* **2014**, *2*, 641.

[65] E. Liu, M. Long, J. Zeng, W. Luo, Y. Wang, Y. Pan, W. Zhou, B. Wang, W. Hu, Z. Ni, *Adv. Funct. Mater.* **2016**, *26*, 1938.